

## NOTES AND CORRESPONDENCE

### Inertial Particle Dynamics in a Hurricane

THEMISTOKLIS SAPSIS AND GEORGE HALLER

*Massachusetts Institute of Technology, Cambridge, Massachusetts*

(Manuscript received 23 June 2008, in final form 8 February 2009)

#### ABSTRACT

The motion of inertial (i.e., finite-size) particles is analyzed in a three-dimensional unsteady simulation of Hurricane Isabel. As established recently, the long-term dynamics of inertial particles in a fluid is governed by a reduced-order inertial equation, obtained as a small perturbation of passive fluid advection on a globally attracting slow manifold in the phase space of particle motions. Use of the inertial equation enables the visualization of three-dimensional inertial Lagrangian coherent structures (ILCS) on the slow manifold. These ILCS govern the asymptotic behavior of finite-size particles within a hurricane. A comparison of the attracting ILCS with conventional Eulerian fields reveals the Lagrangian footprint of the hurricane eyewall and of a large rainband. By contrast, repelling ILCS within the eye region admit a more complex geometry that cannot be compared directly with Eulerian features.

#### 1. Introduction

Our focus here is the dynamics of inertial (i.e., small but finite) particles in the three-dimensional flow field of Hurricane Isabel (cf. Fig. 1). Inertial particles in a fluid are typically modeled as small spherical objects whose velocity differs from the local flow velocity. This difference in velocities is due partly to the mechanical inertia of the particle and partly to viscous drag, buoyancy, and a local alteration of the flow by the particle. All these effects are relevant for the dynamics of dust, droplets, and debris in a hurricane.

Three-dimensional unsteady inertial particle motion satisfies a time-dependent, six-dimensional system of differential equations with a singular perturbation term (see, e.g., Maxey and Riley 1983; Babiano et al. 2000). Understanding the phase space dynamics of this six-dimensional system for a specific fluid flow has not been attempted elsewhere to our knowledge. For this reason, beyond analyzing a specific atmospheric flow, our study also aims to introduce a set of new dynamical systems techniques to the atmospheric literature.

#### *a. Prior work on coherent structures in hurricanes*

Although the prediction of hurricane tracks has considerably improved over the past decades, there is still substantial room for improvement in hurricane intensity forecasting (Houze et al. 2007). In a series of papers (Emanuel 1986, 1988, 1995), Emanuel introduced the energetically based maximum potential intensity (E-MPI) theory to calculate maximal hurricane intensity by employing a frictional boundary layer beneath a conditionally neutral outflow layer. While efficient in some cases, the theory neglects critical aspects of the inner-core structure of mature hurricanes such as Isabel (see, e.g., Montgomery et al. 2006). In general, there is a strong correlation between the storm intensity and the spatial structure of smaller-scale cloud and precipitation features internal to the storm. These features have so far been characterized in terms of conventional meteorological fields, such as temperature, vorticity, and vertical velocity. The Okubo–Weiss and Hua–Klein criteria have also been applied to study the rapid filamentation of convective clouds (Rozoff et al. 2006; Wang 2008) and the geometry of hurricane-like mesovortices (Schubert et al. 1999). Finally, effective diffusivity calculations (Shuckburgh and Haynes 2003) have been employed to identify mixing barriers and regions of efficient wave breaking in 2D hurricane-like vortices (Hendricks and Schubert 2008).

---

*Corresponding author address:* George Haller, Dept. of Mechanical Engineering, Massachusetts Institute of Technology, 77 Massachusetts Ave., Cambridge, MA 02139.  
E-mail: ghaller@mit.edu

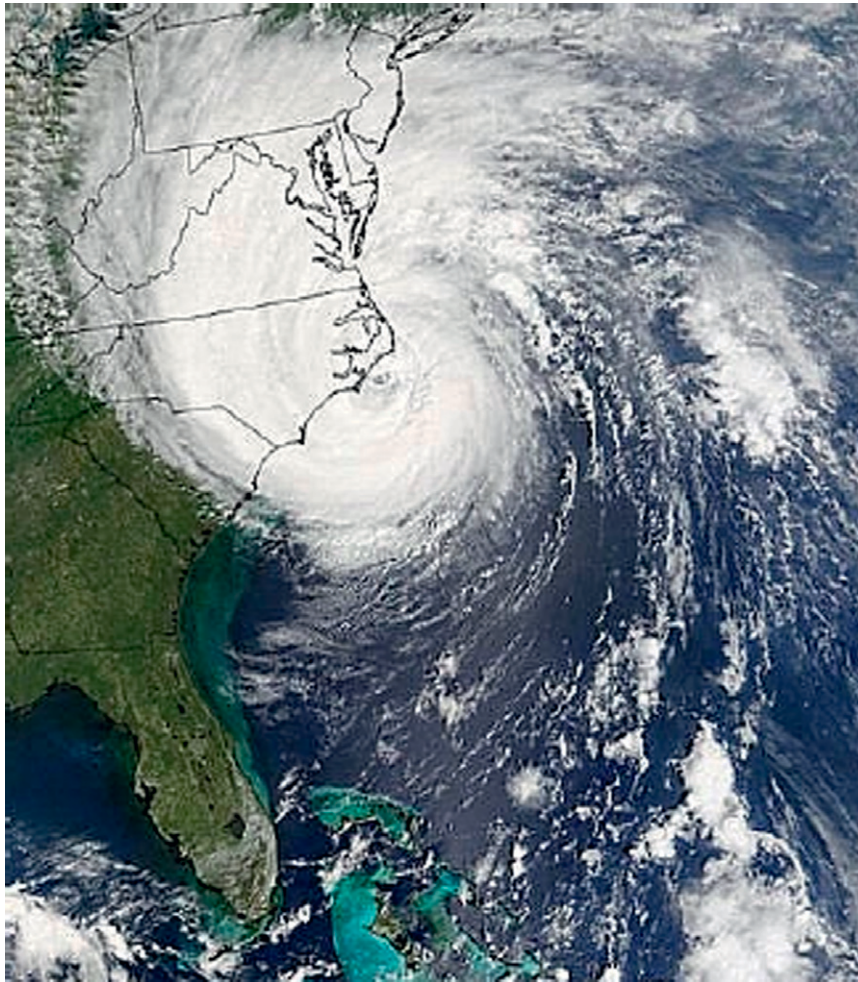


FIG. 1. NASA satellite photo (visible) taken at 11:50 a.m. EDT on 18 Sep 2003 just as the center of Isabel was making landfall.

### *b. Lagrangian coherent structures*

Coherent structures are broadly recognized to play a crucial role in fluid transport, yet an objective (i.e., frame independent) extraction of such structures from velocity data has proven to be challenging. One difficulty is the lack of an accepted definition for coherence in the Eulerian frame: high or low values of vorticity, pressure, strain, and energy have all been suggested as defining quantities (see Jeong and Hussain 1995; Dávila and Vassilicos 2003).

Another difficulty is that typical Eulerian indicators of coherence (such as vorticity and the Okubo–Weiss parameter) are frame dependent (Jeong and Hussain 1995; Haller 2005); that is, they will give different results in frames that rotate relative to each other. Because in unsteady flows with several vortices there is no single distinguished frame, Eulerian coherent structure

criteria are often unsuccessful in capturing intrinsic flow properties.

By contrast, Lagrangian coherent structures (LCS) can be defined as smooth sets of fluid particles with distinguished stability properties. Specifically, repelling LCS are material surfaces that repel all neighboring fluid trajectories; similarly, attracting LCS attract all neighboring fluid trajectories. These definitions are objective, that is, invariant with respect to translations and even time-varying rotations of the coordinate frame. Therefore, LCS can be used to explain the forward and backward time behavior of typical infinitesimal fluid particles.

To extract Lagrangian structures from the flow, one may use the direct Lyapunov exponent (DLE) method developed in (Haller 2001). This method has been applied to laminar flow experiments with periodic (Voth et al. 2002) and aperiodic (Shadden et al. 2006) time dependence, as well as to two-dimensional turbulence experiments

(Mathur et al. 2007) and three-dimensional turbulence simulations (Green et al. 2007). Notably, Mathur et al. (2007) show that attracting and repelling LCS form chaotic tangles in turbulent experimental flows; Green et al. (2007) identify similar tangling structures as the Lagrangian boundaries of three-dimensional hairpin vortices.

### c. Inertial Lagrangian coherent structures in hurricanes

Here we are specifically concerned with an objective identification of observable material structures from the flow field. Observable material structures (such as the eyewall and rainbands) are formed by droplets, dust, and debris (i.e., by inertial particles as opposed to infinitesimal fluid particles). This prompts us to extend the theory of LCS from the infinitesimal particle setting to the finite-size particle setting.

In Haller and Sapsis (2008), we derived a general reduced-order equation (inertial equation) for the asymptotic motion of spherical finite-size particles in unsteady fluid flows. The corresponding reduced inertial velocity field is a small perturbation of the ambient velocity field, with the order of the perturbation defined as the size of the inertial particle relative to characteristic length scales in the flow. Because of this perturbation in velocity, inertial particle motion can develop substantial differences from infinitesimal particle motion in the same ambient flow field.

Here we define inertial Lagrangian coherent structures (ILCS) as LCS extracted from the inertial equation by the DLE method mentioned above. Specifically, attracting ILCS attract finite-size particles, whereas repelling ILCS repel finite-size particles. The network of repelling and attracting ILCS form the inertial analog of tangled networks known from simple examples of chaotic advection of infinitesimal fluid particles.

It turns out, however, that for larger particle sizes, instabilities in the dynamics of inertial particles may develop [Sapsis and Haller 2008b; G. Haller and T. Sapsis (2008, unpublished manuscript, hereafter HASA)]. These instabilities drive away inertial particle trajectories from the slow manifold on which the inertial equation is valid. As a result, in a given flow, an attracting ILCS may only stay attracting for smaller particles, whereas larger particles ultimately spin away from the ILCS because of their inertia. Such spinoffs happen in regions of high strain; the

exact strain threshold is derived in Sapsis and Haller (2008b) for neutrally buoyant particles and in HASA for general particles.

### d. Results

In this paper, we locate key three-dimensional structures that govern dust and droplet dynamics in a hurricane. These structures are 1) attracting ILCS that form visible boundaries between regions of similar particle behavior and 2) repelling ILCS that slice up streams of particles and send them toward different flow regions.

We obtain the ILCS from a reduced three-dimensional (as opposed to six-dimensional) calculation, directly from the inertial equation. For repelling LCS, this is merely a computational advantage. For attracting LCS, use of the inertial equation is a must: the backward-time DLE method applied to the six-dimensional Maxey–Riley equations leads to a numerical blowup due to a strong exponential instability.

In a tropical cyclone, the radius of maximum wind is located in an annular region of heavily precipitating cloud, called the eyewall. This eyewall encircles the relatively calm eye of the storm. Our Lagrangian methods provide a clear and unambiguous (i.e., frame independent) location of the eyewall, as well as of a neighboring rainband, for Hurricane Isabel.

Additionally, applying the results from HASA, we determine the critical particle size over which dynamical instabilities arise in the inertial equation. As a result of these instabilities, larger bodies such as debris or dropsondes will depart from visible surfaces formed by smaller particles, such as droplets and dust.

## 2. Inertial particles dynamics background

Let  $\mathbf{x}$  refer to three-dimensional spatial locations and let  $t$  denote time. Let  $\mathbf{u}(\mathbf{x}, t)$  denote the three-dimensional velocity field of an unsteady flow of density  $\rho_f$ , observed in a rotating coordinate frame with angular velocity  $\mathbf{\Omega}$ . For a spherical particle  $p$  of density  $\rho_p$  and radius  $a$  immersed in the fluid, we denote the particle path by  $\mathbf{x}(t)$ .

Let  $L$  and  $U$  denote a characteristic length scale and a characteristic velocity of the flow, respectively. If the particle is spherical, its Lagrangian velocity  $\dot{\mathbf{x}}(t) = \mathbf{v}(t)$  satisfies the equation of motion (cf. Maxey and Riley 1983; Babiano et al. 2000):

$$\begin{aligned} \rho_p \dot{\mathbf{v}} = & \rho_f \frac{D\mathbf{u}}{Dt} - 2\rho_p \mathbf{\Omega} \times \mathbf{v} + (\rho_p - \rho_f) \mathbf{g} - \frac{9\nu\rho_f}{2a^2} \left( \mathbf{v} - \mathbf{u} - \frac{a^2}{6} \Delta \mathbf{u} \right) - \frac{\rho_f}{2} \left[ \dot{\mathbf{v}} + 2\mathbf{\Omega} \times \mathbf{v} - \frac{D}{Dt} \left( \mathbf{u} + \frac{a^2}{10} \Delta \mathbf{u} \right) \right] \\ & - \frac{9\rho_f}{2a} \sqrt{\frac{\nu}{\pi}} \int_0^t \frac{1}{\sqrt{t-s}} \left[ \dot{\mathbf{v}}(s) + 2\mathbf{\Omega} \times \mathbf{v} - \frac{d}{ds} \left( \mathbf{u} + \frac{a^2}{6} \Delta \mathbf{u} \right)_{\mathbf{x}=\mathbf{x}(s)} \right] ds. \end{aligned} \quad (1)$$

Here  $\rho_p$  and  $\rho_f$  denote the particle and fluid densities, respectively;  $a$  is the radius of the particle;  $\mathbf{g}$  is the constant vector of gravity;  $2\boldsymbol{\Omega} \times \mathbf{v}$  is the Coriolis acceleration including all three components; and  $\nu$  is the kinematic viscosity of the fluid. The individual force terms listed in separate lines on the right-hand side of (1) have the following physical meanings: 1) force exerted on the particle by the undisturbed flow, 2) buoyancy force, 3) Stokes drag, 4) an added mass term resulting from part of the fluid moving with the particle, and 5) Basset–Boussinesq memory term.

The terms involving  $a^2 \Delta \mathbf{u}$  are usually referred to as the Fauxén corrections. For simplicity, we assume that the particle is very small ( $a \ll L$ ), in which case the Fauxén corrections are negligible. We note that the coefficient of the Basset–Boussinesq memory term is equal to the coefficient of the Stokes drag term times  $a/\sqrt{\pi\nu}$ . Therefore, assuming that  $a/\sqrt{\pi\nu}$  is also very small, we neglect the last term in (1), following common practice in the related literature (Michaelides 1997). We finally rescale space, time, and velocity to obtain the simplified equations of motion

$$\begin{aligned} \epsilon \dot{\mathbf{v}} = & \mathbf{u}(\mathbf{x}, t) - \mathbf{v} + \epsilon \frac{3R}{2} \frac{D\mathbf{u}(\mathbf{x}, t)}{Dt} - 2\epsilon \boldsymbol{\Omega} \times \mathbf{v} \\ & + \epsilon \left(1 - \frac{3R}{2}\right) \mathbf{g}, \end{aligned} \quad (2)$$

where

$$\begin{aligned} \epsilon = \frac{1}{\mu} \ll 1, \quad \mu = \frac{R}{St}, \quad R = \frac{2\rho_f}{\rho_f + 2\rho_p}, \quad \text{and} \\ St = \frac{2}{9} \left(\frac{a}{L}\right)^2 Re, \end{aligned}$$

and with  $t$ ,  $\mathbf{v}$ ,  $\mathbf{u}$ ,  $\boldsymbol{\Omega}$ , and  $\mathbf{g}$  now denoting nondimensional variables.

In Eq. (2),  $St$  denotes the particle Stokes number and  $Re = UL/\nu$  is the Reynolds number. The density ratio  $R$  distinguishes neutrally buoyant particles ( $R = 2/3$ ) from aerosols ( $0 < R < 2/3$ ) and bubbles ( $2/3 < R < 2$ ). The  $3R/2$  coefficient represents the added mass effect: an inertial particle brings into motion a certain amount of fluid that is proportional to half of its mass. For neutrally buoyant particles, the equation of motion is simply  $(D/Dt)(\mathbf{v} - \mathbf{u}) = -\mu(\mathbf{v} - \mathbf{u})$ ; that is, the relative acceleration of the particle is equal to the Stokes drag acting on the particle.

Note that (2) is a nonautonomous six-dimensional differential equation. In addition to its temporal and dimensional complexity, (2) also involves a singular perturbation problem because of the small parameter  $\epsilon$  on the left-hand side. This causes a strong exponential instability

when one attempts to solve the equations in backward time to locate attracting invariant manifolds in the six-dimensional phase space (see, e.g., Haller and Yuan 2000).

Haller and Sapsis (2008) proved that for  $\epsilon > 0$  small enough, Eq. (2) written in a nonrotating frame admits a globally attracting invariant slow manifold. This three-dimensional time-dependent surface of particle trajectories can be calculated explicitly up to any order of precision. Inclusion of the Coriolis term does not change this result (Sapsis and Haller 2008a); the slow manifold can then be written in the form

$$\begin{aligned} M_\epsilon = \left\{ (\mathbf{x}, \mathbf{v}_s) : \mathbf{v}_s = \mathbf{u}(\mathbf{x}, t) + \epsilon \left(\frac{3R}{2} - 1\right) \left(\frac{D\mathbf{u}}{Dt} - \mathbf{g}\right) \right. \\ \left. - 2\epsilon \boldsymbol{\Omega} \times \mathbf{u}(\mathbf{x}, t) + \mathcal{O}(\epsilon^2) \right\}, \end{aligned} \quad (3)$$

where  $\{\}$  denotes a set.

At leading order, the dynamics on  $M_\epsilon$  is governed by the inertial equation

$$\dot{\mathbf{x}} = \mathbf{u}(\mathbf{x}, t) + \epsilon \left(\frac{3R}{2} - 1\right) \left(\frac{D\mathbf{u}}{Dt} - \mathbf{g}\right) - 2\epsilon \boldsymbol{\Omega} \times \mathbf{u}(\mathbf{x}, t), \quad (4)$$

a three-dimensional differential equation that has no singular perturbation terms, and hence no associated instability in forward or backward time. Thus, the slow manifold provides us with an Eulerian description of a modified velocity field that governs the motion of inertial particles with given size and density.

In forward time, the inertial equation enables us to track particles efficiently by solving the reduced set of Eq. (4). The forward-time analysis of finite-time Lyapunov exponents allows us to identify repelling Lagrangian structures that are the source of stretching in the flow (cf. below).

In backward time, the inertial Eq. (4) enables the extraction of attracting Lagrangian structures along which particles congregate to form observable patterns (cf. below). Still in backward time, (3) allows for source inversion, that is, the identification of a source from which a dispersed set of particles was originally released.

Note that for  $\epsilon = 0$  (infinitesimally small particles), the inertial equation is reduced to the equation of motion for fluid particles. Hence, finite-size particle motion is a small perturbation of passive fluid advection. Also observe that the effects of gravity, the Coriolis force, and force exerted by the flow are of the same order  $\epsilon$ . This sheds some doubt on the accuracy of ignoring all forces but gravity on the particle, a common approximation in the weather literature. This approximation appears to be least justifiable near high-velocity and high-strain regions, such as the eyewall.

For larger values of  $\varepsilon$ , the slow manifold  $M_\varepsilon$  will start losing its stability on larger and larger spatial domains. Sapsis and Haller (2008b) and HASA show that such instabilities develop at high-strain regions of  $M_\varepsilon$  that violate the stability condition

$$s(\mathbf{x}, t) \equiv \lambda_{\max} \left[ -\frac{\mathbf{V}\mathbf{v}_s(\mathbf{x}, t) + [\mathbf{V}\mathbf{v}_s(\mathbf{x}, t)]^T}{2} \right] - \frac{1}{\varepsilon} < 0; \quad (5)$$

here  $\lambda_{\max}[A]$  denotes the maximal eigenvalue of a tensor  $A$ ;  $A^T$  is the transpose of  $A$ ; and  $\mathbf{V}\mathbf{v}_s(\mathbf{x}, t) = \mathbf{V}\mathbf{u}(\mathbf{x}, t) + \varepsilon(3R/2 - 1)\mathbf{V}(D\mathbf{u}/Dt) - 2\varepsilon\boldsymbol{\Omega} \times \mathbf{V}\mathbf{u}(\mathbf{x}, t)$ .

### 3. Hurricane Isabel dataset

#### a. Hurricane overview

Isabel formed from a tropical wave that moved westward from the coast of Africa on 1 September. Over the next several days, the wave moved slowly westward and gradually became better organized. Isabel turned west-northwestward on 7 September, intensifying into a hurricane. Its strengthening continued for the next two days while it moved between west-northwest and northwest. Isabel turned westward on 10 September, then maintained its direction until 13 September on the south side of the Azores–Bermuda high.

Isabel subsequently strengthened to a category-5 hurricane on 11 September, with maximum sustained winds estimated at 145 kt at 1800 UTC that day. After this peak, the maximum winds remained in the 130–140-kt range until 15 September. During this time, Isabel displayed a persistent eye of 35–45 nautical miles in diameter. Isabel approached a weakness in the western portion of the Azores–Bermuda high, which allowed the hurricane to turn west-northwestward on 13 September, northwestward on 15 September, and north-northwestward on 16 September. The latter motion would continue for the rest of Isabel's life as a tropical cyclone.

Increased vertical wind shear on 15 September caused Isabel to gradually weaken. The system weakened below major hurricane status (96 kt or category 3 on the Saffir–Simpson scale) on 16 September. It maintained category-2 status with 85–90-kt maximum winds for the next two days, while the overall size of the hurricane increased. During that time, Isabel's intensity is somewhat uncertain as a large outer eyewall was formed, which disrupted the inner core wind structure (Beven and Cobb 2003). Isabel made landfall near Drum Inlet, North Carolina, around 1700 UTC on 18 September as a category-2 hurricane and then weakened as it moved across eastern North Carolina.

#### b. The dataset

The numerical data we use here for the velocity field  $\mathbf{u}(\mathbf{x}, t)$  and for other Eulerian quantities describe Hurricane Isabel from 1700 UTC 16 September 16 until 1700 UTC 18 September. The data was produced by the Weather Research and Forecast (WRF) model, courtesy of the national center for Atmospheric Research (NCAR), and the U.S. National Science Foundation (NSF). Details for the WRF model can be found in Skamarock et al. (2005).

The simulation covers a period of 48 time steps (hours), where time steps refer to model output times. Each time step contains the instantaneous velocity field with a grid resolution of  $500 \times 500 \times 100$  and horizontal grid spacing of 4 km, covering an atmospheric volume with coordinates running from  $83^\circ\text{W}$  to  $62^\circ\text{W}$  (longitude:  $x$  axis),  $23.7^\circ\text{N}$  to  $41.7^\circ\text{N}$  (latitude:  $y$  axis), and 0.035 km to 19.835 km (height:  $z$  axis).

To nondimensionalize the data, we choose the characteristic length scale  $L = 10$  km, the characteristic velocity  $U = 10$  m s $^{-1}$ , and the characteristic time scale  $T = L/U = 1000$  s. The earth rotates with angular velocity  $\boldsymbol{\Omega}$ , which we will take for our analysis to be constant and equal to  $T \times 7.29 \times 10^{-5}$  s $^{-1}$ .

### 4. Slow manifold in the flow

We first determine the critical value of  $\varepsilon$  below which the inertial Eq. (4) governs inertial particle dynamics (i.e., the slow manifold  $M_\varepsilon$  attracts exponentially all finite-size particle trajectories). To this end, we compute the quantity  $s(\mathbf{x}, t)$  at  $t = 18$  for two different values of  $\varepsilon$  (Fig. 2). The space enclosed by the blue surfaces indicates regions of instability, where the inequality (5) is violated, and hence particle velocities diverge from those observed at the same spatial location on the slow manifold  $M_\varepsilon$ . Note that for  $\varepsilon = 0.1$ , the unstable high-strain regions are small and therefore the inertial equation governs particle asymptotics practically everywhere. For reference, this value of  $\varepsilon$  corresponds to objects of a typical diameter  $d = 10$  cm in our flow. Thus, the instability of the slow manifold mainly concerns particles of larger size such as dropsondes, which are dropped from high altitude to obtain data on hurricanes. On the other hand, common meteorological species such as dust or raindrops converge rapidly on the slow manifold, and the motion in this case is described completely by the inertial equation.

Now we show that for small enough  $\varepsilon$  values, the slow manifold  $M_\varepsilon$  indeed gives the correct asymptotic motion of finite-size particles when compared with the Maxey–Riley equations. For particles, we choose aerosols with

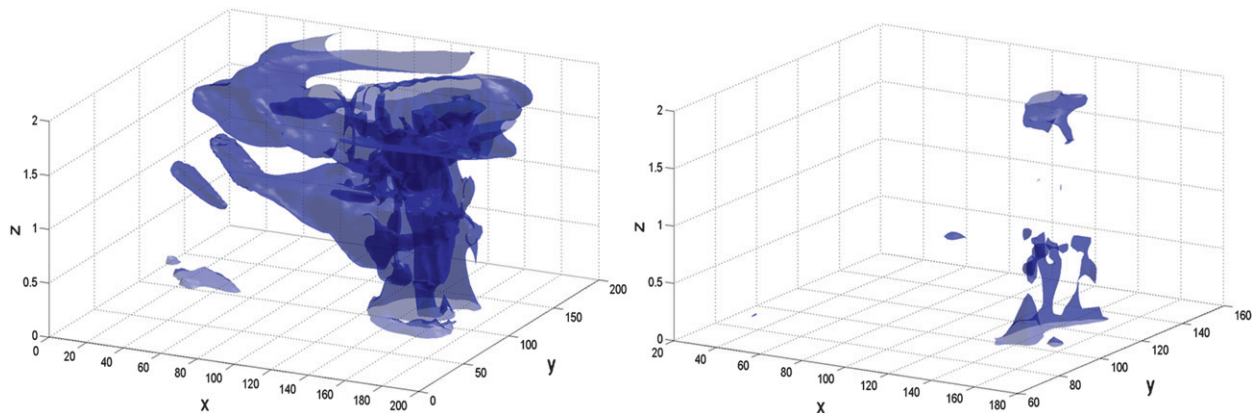


FIG. 2. Unstable regions at  $t = 18$  for aerosols ( $R = 0.5$ ) with (left)  $\epsilon = 0.2$  and (right)  $\epsilon = 0.1$ . The axes here and hereafter are in nondimensional units (with characteristic length  $L = 10$  km) and the center of the hurricane is located at  $(145, 120)$ .

parameters  $R = 10^{-3}$  and  $\epsilon = 10^{-3}$  that describe raindrops. We solve the full six-dimensional Maxey–Riley Eq. (2) on the time interval  $[17, 18]$  using a fourth-order Runge–Kutta algorithm with absolute integration tolerance  $10^{-6}$ . The initial velocity of the particle was taken to be much larger in absolute value than the velocity corresponding to the same initial location on the slow manifold; this is to illustrate the rapid convergence of order  $\mathcal{O}(1/\epsilon)$  of particle paths to the slow manifold.

In Fig. 3, we show the projection of the six-dimensional solution of (2) onto the  $\{x, y, |\mathbf{v}|, z_p(t), (t)\}$  space, where  $z_p(t)$  is the instantaneous  $z$  coordinate of the particle. We also show the slow manifold  $M_\epsilon$  (blue surface); we use color to indicate the third dimension of  $M_\epsilon$ , computed at  $t = 18$  at the instantaneous vertical particle position  $z_p(t)$ . Specifically, colors ranging from dark blue to dark red indicate increasing values of  $|\mathbf{v}| =$

$|\mathbf{u}[\cdot, \cdot, z_p(t), T]|$ , which is a measure of the “height” of the three-dimensional slow manifold at leading order in the full  $(\mathbf{x}, \mathbf{v})$  coordinate space. Note the rapid exponential convergence of the particle trajectory to  $M_\epsilon$ .

### 5. Inertial Lagrangian coherent structures

#### a. Extraction of ILCS

Lagrangian coherent structures are distinguished sets of fluid trajectories that govern the forward- and backward-time asymptotics of other fluid particles. They can be located by calculating direct Lyapunov exponents (see below) from the Lagrangian equation of motion  $\dot{\mathbf{x}} = \mathbf{u}(\mathbf{x}, t)$  for infinitesimal particles (see, e.g., Haller and Yuan 2000; Lekien et al. 2007; Shadden et al. 2005; Mathur et al. 2007). The DLE method has several

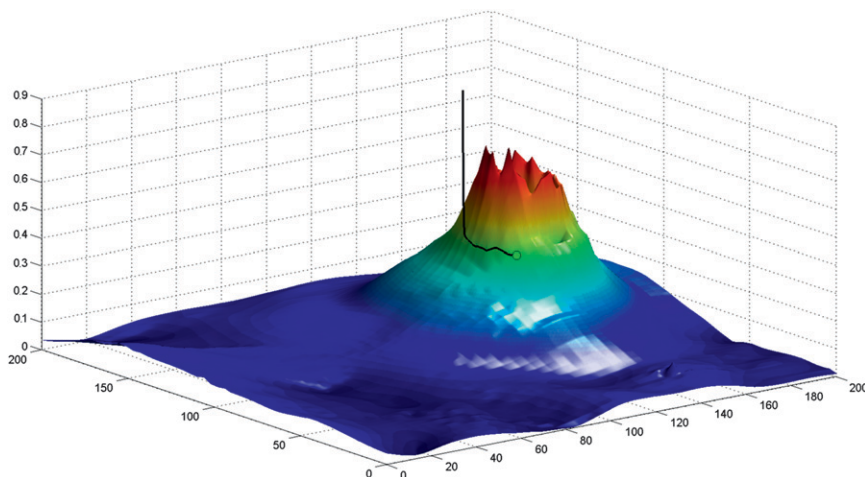


FIG. 3. Convergence of an inertial particle (aerosol) to the slow manifold  $M_\epsilon$  shown in the  $(x, y, |\mathbf{v}|)$  space at  $t = 18$ . The particle is advected under the full Maxey–Riley equation; the slow manifold is computed directly from the analytic Eq. (2).

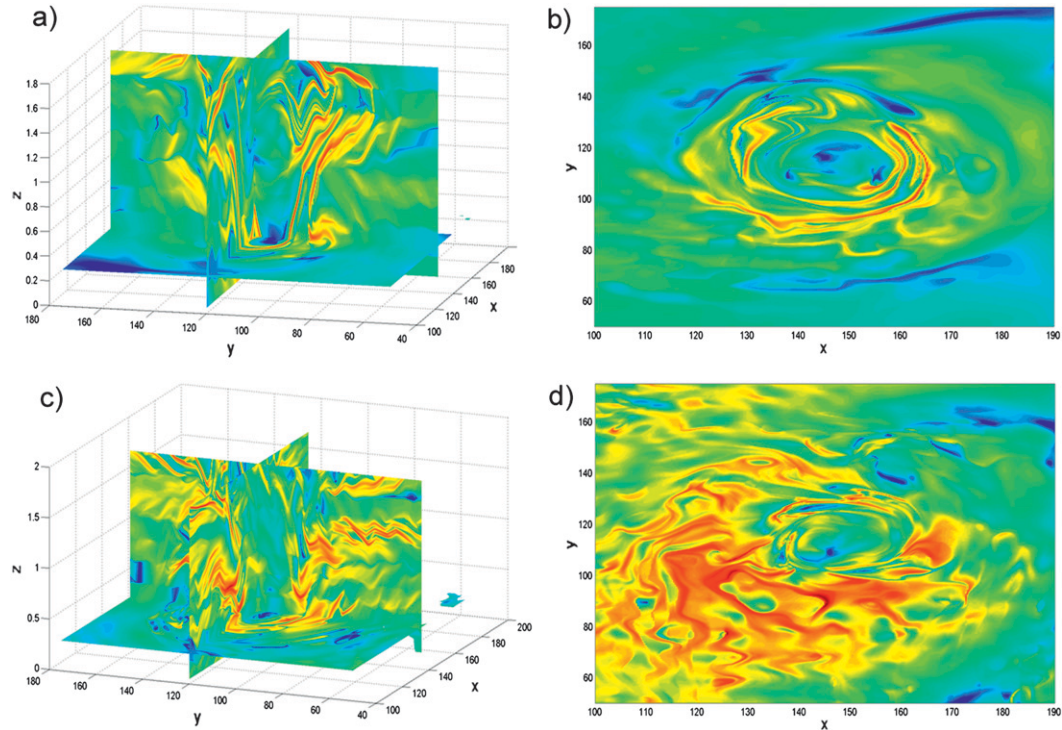


FIG. 4. (a) Backward-time DLE field close to the core of the hurricane for  $t_0 = 18$  and aerosols with  $R = 10^{-3}$  and  $\epsilon = 10^{-3}$ ; (b)  $z$  section of the backward DLE field for  $z = 1$ . (c),(d) As in (a),(b), respectively, but for the forward-time DLE field. For all the plots shown red regions indicate the lower-dimensional manifolds where the DLE reaches its maximum value.

advantages over Eulerian methods, including frame independence, greater detail, and the ability to define structure boundaries without relying on a preselected threshold. On the downside, as with all Lagrangian methods, DLE relies on the generation of particle paths and hence is more computationally intensive than Eulerian methods.

As an advance in the current paper, we locate LCS that impact the motion of finite-size particles. Such inertial LCS are obtained by applying the DLE method to the inertial Eq. (4). Note that ILCS differ from LCS in that the latter are calculated for the infinitesimal particle dynamics governed by  $\dot{\mathbf{x}} = \mathbf{u}(\mathbf{x}, t)$ . Such classic LCS were computed recently by Du Toit et al. (2007) for a two-dimensional hurricane model.

By solving numerically the inertial Eq. (4) for a grid of initial conditions  $\mathbf{x}_0$  at  $t_0$ , we determine the asymptotic inertial particle trajectories  $\mathbf{x}(t, \mathbf{x}_0)$ . For the numerical solution of the inertial equation, a fourth-order Runge–Kutta algorithm is combined with a cubic interpolation scheme for both space and time to improve resolution of the dataset. As initial time, we choose  $t_0 = 18$ ; the integration time interval is chosen for both backward and forward integration  $\Delta T = 5$ . By numerical differentiation,

we compute the largest singular-value field  $\lambda_{\max}(t, t_0, \mathbf{x}_0)$  of the deformation-gradient tensor field  $\partial \mathbf{x}(t, t_0, \mathbf{x}_0) / \partial \mathbf{x}_0$ . We then use the local maximizing sets of the DLE field  $\sigma_{t_0}^i(\mathbf{x}_0) = [\ln \lambda_{\max}(t, t_0, \mathbf{x}_0)] / \geq [2(t - t_0)]$ , plotted over initial positions  $\mathbf{x}_0$ , to visualize the ILCS.

#### b. Identification of hurricane structures through ILCS

In Figs. 4a,b and 4c,d, we present various sections of the scalar backward and forward DLE field, respectively. Red regions indicate the lower-dimensional surfaces where the DLE reaches its maximum value; these ridges coincide with attracting ILCS in the backward-time case and with repelling ILCS in the forward-time case.

In Fig. 5 we compare the backward DLE field with various conventional meteorological fields including vertical velocity, vorticity, the Okubo–Weiss criterion, rain mixing ratio, and cloud mixing ratio. Note that the main attracting ILCS in the hurricane consist of the local maximizing surfaces shown in Fig. 6a. The central cylindrical sheath depicts the eyewall, as confirmed by the strong correlation between the horizontal Eulerian fields (Fig. 5) and the local maximizing curves of the

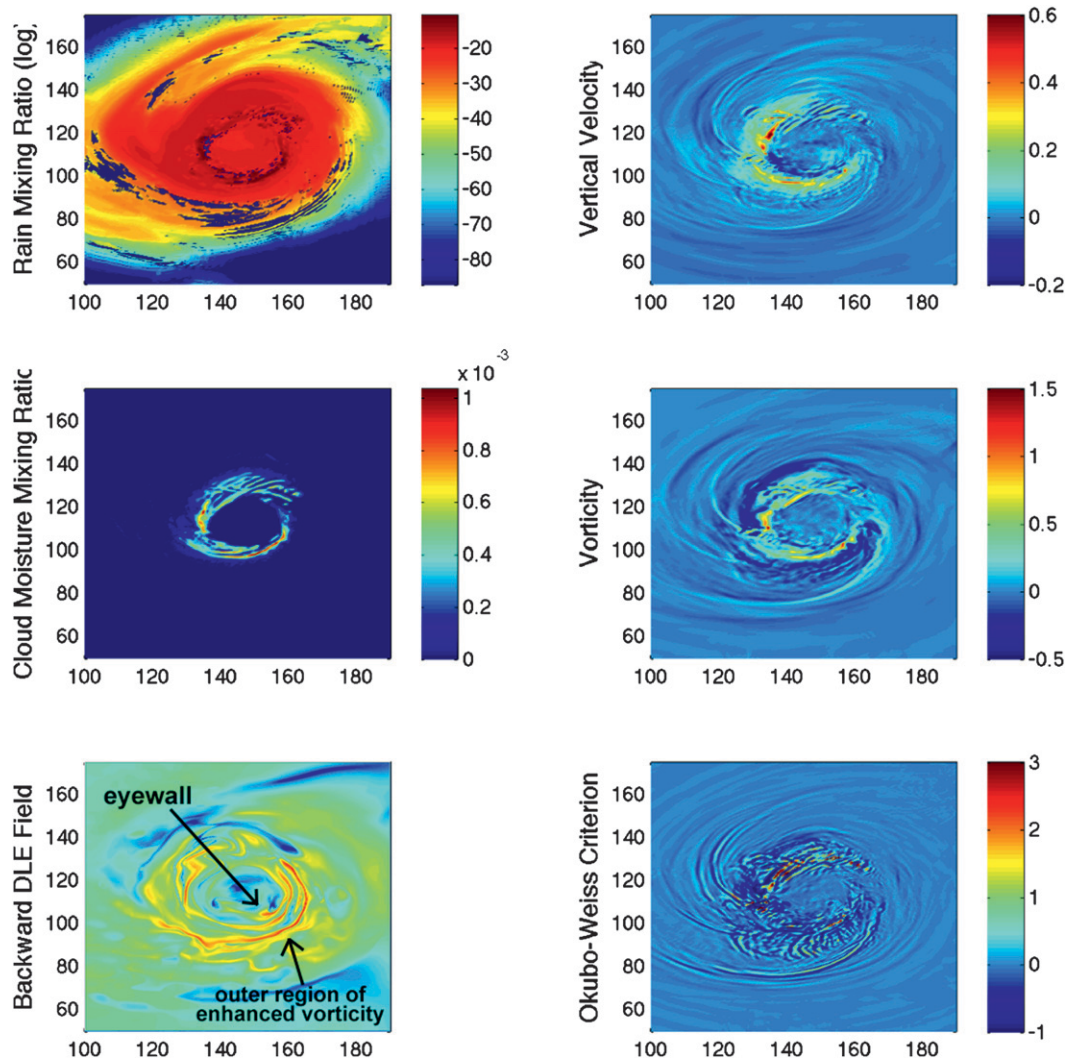


FIG. 5. Horizontal sections of rain mixing ratio ( $\text{kg kg}^{-1}$ ), vertical velocity (nondimensionalized with  $U$ ), cloud mixing ratio ( $\text{kg kg}^{-1}$ ), potential vorticity (nondimensionalized with  $U/L$ ), backward DLE field, and Okubo-Weiss criterion [nondimensionalized with  $(U/L)^2$ ] for  $z = 1$ .

backward DLE field. We note the sharpness of the eyewall (Fig. 6a) relative to the pictures provided by Eulerian indicators such as the Okubo-Weiss criterion (Fig. 5).

In Figs. 4b and 6a, we can also observe an outer concentric “mantle” positioned across the northern azimuths of the storm, emerging from the core region of the hurricane near the west azimuths. We note that the above structure is strongly correlated with both the Okubo-Weiss criterion and the potential vorticity (Fig. 5) as well as with the rain mixing ratio. Specifically, by comparing the backward DLE field (Fig. 4b or 5) with the rain mixing ratio (Fig. 5), we observe that this outer concentric mantle is on the boundary that separates two rainbands having coordinates (120, 80) and (130, 100). Additionally, a calculation of the 200–850-mb vertical

wind shear (method described in Emanuel et al. 2004) shows that Isabel was experiencing a strong westerly wind shear of  $11.2 \text{ m s}^{-1}$ . As was found in Corbosiero and Molinari (2002), there is a strong correlation between the azimuthal distribution of convection and the direction of the vertical wind shear, suggesting that this outer structure is correlated with the boundary of a large rainband. Although Beven and Cobb (2003) report the formation of a large outer eyewall, this cannot be fully confirmed from either the ILCS or the Eulerian indicators, probably because of insufficient accuracy of the hurricane simulation to reproduce all the structures that are apparent in the real storm. Hence, based on the simulated data, the above asymmetric structure may be the Lagrangian signature of a vortex Rossby wave



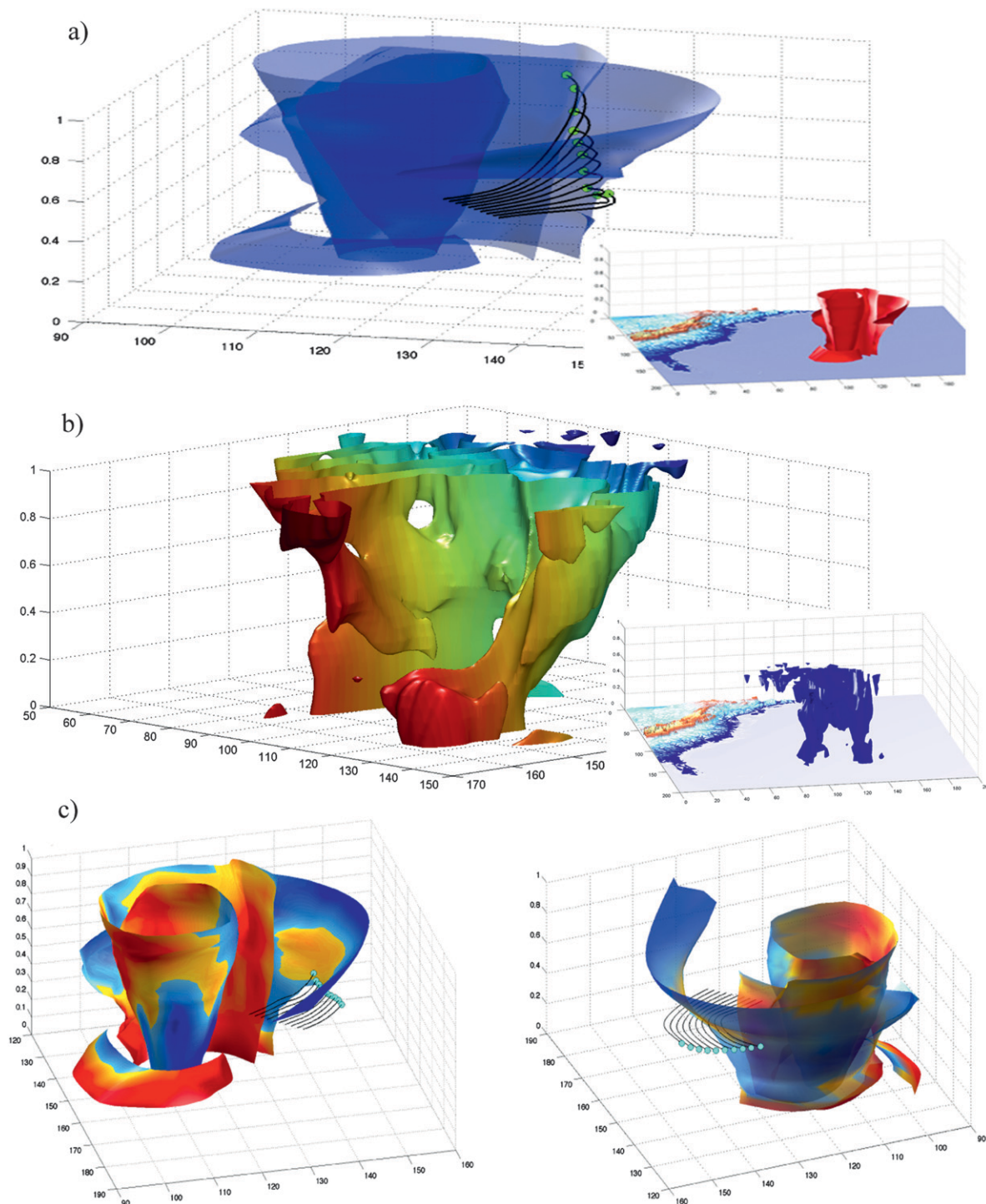


FIG. 6. (a) Attracting manifold at  $t_0 = 18$  extracted from the inertial equation as ridges of the backward-time DLE fields. Green particles are aerosols with  $\epsilon = 0.1$  for which the slow manifold is attracting. (b) Repelling manifold consisting of the set of points for which the DLE is greater than 80% of its maximum value. The coloring is with respect to the spatial  $x$  variable to illustrate the three-dimensionality of the objects involved. (c) Attracting ILCS computed through the inertial equation and colored according to stability criterion (4) for  $\epsilon = 0.2$ . (Red regions on the ILCS indicate locations where the velocities of the inertial particles will diverge from the velocity field induced by the slow dynamics; blue regions indicate locations where the velocity of inertial particles will be described accurately by the slow manifold).

previously studied in Möller and Montgomery (1999, 2000) or a convectively coupled vortex Rossby wave studied in Schecter and Montgomery (2007).

Ridges of the forward-time DLE field correspond to repelling ILCS that are not highlighted by particle accumulation. Still, they play a crucial role in organizing horizontal and vertical mixing in the flow. In the flow field of Isabel, repelling ILCS display a more complex structure than attracting ILCS. Specifically, repelling ILCS appear to consist of local DLE maximizer sets that are not always smooth two-dimensional submanifolds (surfaces) (Fig. 4d). Hence, the extraction of repelling ILCS as maximizing two-dimensional surfaces is not always feasible; instead, the repelling ILCS are shown as the set of points with DLE greater than 80% of its maximum value (Fig. 6b). The coloring we use for repelling ILCS is with respect to the spatial  $x$  variable to illustrate the three-dimensionality of the objects involved.

The altitude corresponding to Fig. 4d (i.e.,  $z = 10$  km) is the beginning of the outflow jet and therefore the complex repelling structures shown in Fig. 4d are correlated with the strong shear from the structure of the hurricane on the underside of the outflow jet. Although repelling ILCS generally possess a complicated structure, this is not the case inside the hurricane eyewall where well-defined structures can be observed (Figs. 4c,d). These structures play the role of mixing barriers, which are determined in Hendricks and Schubert (2008) using the method of effective diffusivity. This method is an established diagnostic tool (Shuckburgh and Haynes 2003) but does not reveal the specific, highly tangled, geometric structure of the flow in as much detail as ILCS does. In particular, inertial particles are subject to repulsion by repelling ILCS and simultaneously attraction by attracting ILCS. Therefore, the complex tangle formed by these two sets of manifolds defines the global

geometry of the flow, revealing the locations that inertial particles came from and will move to. Using the geometry of the ILCS, one should be able to describe and quantify small-scale mixing and transport in hurricane cores, such as mixing between the eye and the eyewall (Cram et al. 2007) or entrainment of high-entropy air into the eyewall, a process related to superintensity (Persing and Montgomery 2003). All this will undoubtedly require higher-resolution data.

### c. Inertial particles in the flow

In Fig. 6a, we show the trajectories of a set of inertial particles released near the hurricane (with green dots denoting the end of those trajectories) and then advected using the full Maxey–Riley equation [(2)]. This set of particles are aerosols with  $R = 0.5$  and  $\varepsilon = 0.1$  (parameters that correspond to a typical dropsonde) for which the slow manifold is stable almost everywhere (see Fig. 2, right). Accordingly, we observe their rapid converge to the attracting ILCS we have computed.

In Fig. 6c, we show the ILCS computed using the inertial equation for  $\varepsilon = 0.2$ , colored according to the stability criterion [(5)] for the same value of  $\varepsilon$ . Specifically, red regions on the ILCS indicate locations where the velocities of the inertial particles will diverge from the velocity field induced by the slow dynamics, whereas blue regions indicate locations where the ILCS computed through the slow dynamics will indeed attract finite-size particles with  $\varepsilon = 0.2$ .

The complete three-dimensional description of the stability regions for inertial particles with  $\varepsilon = 0.2$  is given in Fig. 2 (left). In Fig. 6c (left), we show a set of inertial particles ( $R = 0.5$  and  $\varepsilon = 0.2$ ) initialized near a blue region of the ILCS. Observe that these particles tend to align with the ILCS. In Fig. 6c (right) we choose to initialize another set of inertial particles in a different location where an instability of the slow manifold is

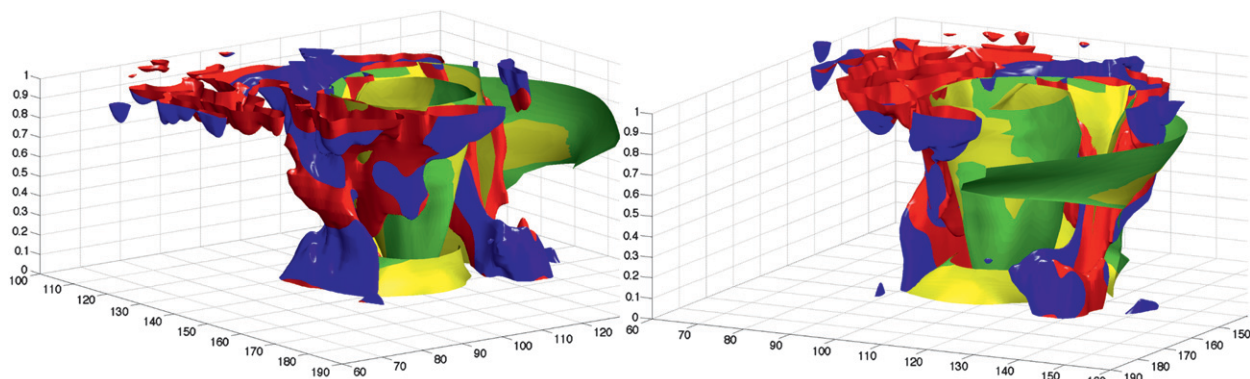


FIG. 7. ILCS for  $\varepsilon = 0.2$  from two different viewing angles. Yellow (red) regions indicate the parts of the attracting (repelling) ILCS where inertial particle velocity will diverge from the slow manifold. Green (blue) regions indicate the parts of the attracting (repelling) ILCS where particles' velocity will converge to the slow manifold velocity exponentially fast.

predicted by Eq. (5). Observe that these particles cross the projection of ILCS and then subsequently (when they approach a stable region of the slow manifold) align with the ILCS.

In Fig. 7, we show both the attracting and repelling ILCS from two different view angles, colored according to the stability criterion (5) for  $\varepsilon = 0.2$ . More specifically, yellow (red) regions indicate the parts of the attracting (repelling) ILCS where inertial particle velocity will diverge from the velocity field given by the slow manifold; over these regions the extracted ILCS will not govern the motion of inertial particles. On the other hand, green (blue) regions indicate the parts of the attracting (repelling) ILCS where particle velocities will converge to the slow manifold velocity exponentially fast. Thus, over these regions the extracted ILCS will efficiently describe the motion of inertial particles.

The differences between the ILCS computed for different  $\varepsilon$  values (e.g., Figs. 6a,c) are not significant. However, individual particle behavior differs dramatically in the two cases in accordance with the different stability properties of the slow manifold. This confirms that ILCS computed for the inertial equation are the relevant governing structures for finite-size particle motion, as long as the particles are small enough to satisfy the stability criterion (5).

## 6. Conclusions

In this work we have identified inertial Lagrangian coherent structures (ILCS) that govern the motion of inertial particles in a numerical model of Hurricane Isabel. Through a slow manifold reduction and the numerical solution of the corresponding inertial equation, we have calculated the backward- and forward-time direct Lyapunov exponent (DLE) fields on the slow manifold. The ridges of these scalar fields mark the location of attracting and repelling ILCS, respectively. Additionally, we have determined the critical size of inertial particles below which ILCS derived from the inertial equation govern the asymptotic particle motion in forward and backward time.

The attracting ILCS we have identified are consistent with features observed in more conventional meteorological fields, such as potential vorticity, rain mixing ratio, and the Okubo–Weiss criterion. Through a comparison of the attracting ILCS and Eulerian quantities, we have identified the eyewall of the hurricane as well as an outer region of enhanced vorticity that is strongly correlated with a large rainband caused by a vertical wind shear.

By contrast, repelling ILCS (which create mixing and disperse particles toward various attracting ILCS) show

a more complex geometry. Because of their instability, repelling ILCS are not directly observable in flow experiments, and hence their detailed topology and implications on global mixing within a hurricane deserves further numerical study.

*Acknowledgments.* This research was supported by NSF Grant DMS-04-04845, AFOSR Grant AFOSR FA 9550-06-0092, and a George and Marie Vergottis Fellowship at MIT. The authors would also like to thank the anonymous reviewers for their helpful comments that led to a number of improvements.

## REFERENCES

- Babiano, A., J. H. E. Cartwright, O. Piro, and A. Provenzale, 2000: Dynamics of a small neutrally buoyant sphere in a fluid and targeting in Hamiltonian systems. *Phys. Rev. Lett.*, **84**, 5764–5767.
- Beven, J., and H. Cobb, cited 2003: Tropical cyclone report: Hurricane Isabel. National Hurricane Center, National Weather Service. [Available online at <http://www.nhc.noaa.gov/2003isabel.shtml>]
- Corbosiero, K. L., and J. Molinari, 2002: The effects of vertical wind shear on the distribution of convection in tropical cyclones. *Mon. Wea. Rev.*, **130**, 2110–2123.
- Cram, T. A., J. Persing, M. T. Montgomery, and S. A. Braun, 2007: A Lagrangian trajectory view on transport and mixing processes between the eye, eyewall, and environment using a high resolution of Hurricane Bonnie (1998). *J. Atmos. Sci.*, **64**, 1835–1856.
- Dávila, J., and J. C. Vassilicos, 2003: Richardson's pair diffusion and the stagnation point structure of turbulence. *Phys. Rev. Lett.*, **91**, 144501, doi:10.1103/PhysRevLett.91.144501.
- Du Toit, P. C. D., J. E. Marsden, and S. S. Chen, 2007: Visualizing and quantifying transport in hurricanes. *Eos, Trans. Amer. Geophys. Union*, **88** (Fall Meeting Suppl.), Abstract A21C-0647.
- Emanuel, K. A., 1986: An air–sea interaction theory for tropical cyclones. Part I: Steady-state maintenance. *J. Atmos. Sci.*, **43**, 585–605.
- , 1988: The maximum intensity of hurricanes. *J. Atmos. Sci.*, **45**, 1143–1155.
- , 1995: Sensitivity of tropical cyclones to surface exchange coefficients and a revised steady-state model incorporating eye dynamics. *J. Atmos. Sci.*, **52**, 3969–3976.
- , C. DesAutels, C. Holloway, and R. Korty, 2004: Environmental control of tropical cyclone intensity. *J. Atmos. Sci.*, **61**, 843–858.
- Green, M. A., C. W. Rowley, and G. Haller, 2007: Detection of Lagrangian coherent structures in 3D turbulence. *J. Fluid Mech.*, **572**, 111–120.
- Haller, G., 2001: Distinguished material surfaces and coherent structures in 3D fluid flows. *Physica D*, **149**, 248–277.
- , 2005: An objective definition of a vortex. *J. Fluid Mech.*, **525**, 1–26.
- , and G. Yuan, 2000: Lagrangian coherent structures and mixing in two-dimensional turbulence. *Physica D*, **147**, 352–370.
- , and T. Sapsis, 2008: 'Where do inertial particles go in fluid flows?' *Physica D*, **237**, 573–583.
- Hendricks, E., and W. H. Schubert, 2008: Aspects of chaotic mixing in the hurricane inner-core. Preprints, *28th Conf. on Hurricanes and Tropical Meteorology*, Orlando, FL, Amer.

- Meteor. Soc., 14C.2. [Available online at <http://ams.confex.com/ams/pdfpapers/138212.pdf>.]
- Houze, R. A., S. S. Chen, B. Smull, W. C. Lee, and M. Bell, 2007: Hurricane intensity and eyewall replacement. *Science*, **315**, 1235–1239.
- Jeong, J., and F. Hussain, 1995: On the identification of a vortex. *J. Fluid Mech.*, **285**, 69–94.
- Lekien, F., S. Shadden, and J. Marsden, 2007: Lagrangian coherent structures in  $n$ -dimensional systems. *J. Math. Phys.*, **48**, 1–19.
- Mathur, M., G. Haller, T. Peacock, J. Ruppert-Felsot, and H. Swinney, 2007: Uncovering the Lagrangian skeleton of turbulence. *Phys. Rev. Lett.*, **98**, 144502, doi:10.1103/PhysRevLett.98.144502.
- Maxey, M. R., and J. J. Riley, 1983: Equation of motion for a small rigid sphere in a nonuniform flow. *Phys. Fluids*, **26**, 883–889.
- Michaelides, E. E., 1997: The transient equation of motion for particles, bubbles, and droplets. *J. Fluids Eng.*, **119**, 233–247.
- Möller, J. D., and M. T. Montgomery, 1999: Vortex Rossby waves and hurricane intensification in a barotropic model. *J. Atmos. Sci.*, **56**, 1674–1687.
- , and —, 2000: Tropical cyclone evolution via potential vorticity anomalies in a three-dimensional balance model. *J. Atmos. Sci.*, **57**, 3366–3387.
- Montgomery, M. T., M. M. Bell, S. M. Aberson, and M. L. Black, 2006: Hurricane Isabel (2003): New insights into the physics of intense storms. Part I: Mean vortex structure and maximum intensity estimates. *Bull. Amer. Meteor. Soc.*, **87**, 1335–1347.
- Persing, J., and M. T. Montgomery, 2003: Hurricane superintensity. *J. Atmos. Sci.*, **60**, 2349–2371.
- Rozoff, C. M., W. H. Schubert, B. D. McNoldy, and J. P. Kossin, 2006: Rapid filamentation zones in intense tropical cyclones. *J. Atmos. Sci.*, **63**, 325–340.
- Sapsis, T., and G. Haller, 2008a: Inertial particle's motion in geophysical fluid flows. *Proc. Sixth EUROMECH Nonlinear Dynamics Conf.*, St. Petersburg, Russia, European Mechanics Society, 1–7.
- , and —, 2008b: Instabilities in the dynamics of neutrally buoyant particles. *Phys. Fluids*, **20**, 017102, doi:10.1063/1.2830328.
- Schecter, D. A., and M. T. Montgomery, 2007: Waves in a cloudy vortex. *J. Atmos. Sci.*, **64**, 314–337.
- Schubert, W. H., M. T. Montgomery, R. K. Taft, T. A. Guinn, S. R. Fulton, J. P. Kossin, and J. P. Edwards, 1999: Polygonal eyewalls, asymmetric eye contraction, and potential vorticity mixing in hurricanes. *J. Atmos. Sci.*, **56**, 1197–1223.
- Shadden, S. C., F. Lekien, and J. E. Marsden, 2005: Definition and properties of Lagrangian coherent structures: Mixing and transport in two-dimensional aperiodic flows. *Physica D*, **212**, 271–304.
- , J. O. Dabiri, and J. E. Marsden, 2006: Lagrangian analysis of fluid transport in empirical vortex ring flows. *Phys. Fluids*, **18**, 047105, doi:10.1063/1.2189885.
- Shuckburgh, E., and P. Haynes, 2003: Diagnostic transport and mixing using a tracer-based coordinate system. *Phys. Fluids*, **15**, 3342–3357.
- Skamarock, W. C., J. B. Klemp, J. Dudhia, D. O. Gill, D. M. Barker, W. Wang, and J. G. Powers, 2005: A description of the Advanced Research WRF version 2. NCAR Tech. Note NCAR/TN-468+STR, 88 pp.
- Voth, G. A., G. Haller, and J. Gollub, 2002: Experimental measurements of stretching fields in fluid mixing. *Phys. Rev. Lett.*, **88**, 254501, doi:10.1103/PhysRevLett.88.254501.
- Wang, Y., 2008: Rapid filamentation zone in a numerically simulated tropical cyclone. *J. Atmos. Sci.*, **65**, 1158–1181.